COMPUTATIONAL INVESTIGATION OF HYDRO-MECHANICAL EFFECTS ON TRANSMISSIVITY EVOLUTION DURING THE INITIAL INJECTION PHASE AT THE DESERT PEAK EGS PROJECT, NV

Stefano Benato[1], Donald M. Reeves [1], Rishi Parashar [1], Nicholas C. Davatzes [2], Stephen Hickman [3], Derek Elsworth [4], Paul Spielman [5], Joshua Taron [3]

1 - Division of Hydrologic Sciences, Desert Research Institute, Reno, NV, 89512 USA

2 - Temple University, Philadelphia, PA, 19122 USA

3 - U.S. Geological Survey, Menlo Park, CA, 94025 USA

4 - Pennsylvania State University, University Park, PA, 16802 USA

5 - Ormat Nevada Inc., Reno, NV, 89511 USA

stefano.benato@dri.edu

ABSTRACT

The low-flow-rate injection phase of an Engineered Geothermal System (EGS) experiment in Desert Peak well 27-15 produced increased injectivity at wellhead pressures less than the minimum principal stress, consistent with hydraulically induced mechanical shear failure in the surrounding rock. We use statistical fracture analysis and hydro-mechanical modeling to simulate the observed pressure response during this shear stimulation, to explore one possible conceptual framework for the overall Desert Peak EGS experiment. This is part of a long-term study to simulate the complete Desert Peak EGS stimulation, including both shearing and hydraulic fracturing (tensile) failure.

Discrete fracture network simulations, based on fracture/fault attributes measured downhole and at the surface, were used to derive equivalent permeability tensors for comparison with preferred fluid migration directions observed in hydraulic and tracer tests. FLAC^{3D}, a hydro-mechanical simulator, was used to investigate changes in stress and displacement according to a Mohr-Coulomb frictional model subjected to perturbations in pore pressure. Although almost all of the seismicity observed during the EGS stimulation occurred during the high-flow-rate tensile stimulation phase, we use this seismicity to illuminate the geometry of large-scale geologic structures that could also have served as preferential flow paths during shear stimulation. This analysis shows that conditions for shear failure during the low-flow-rate shear stimulation could occur in locations consistent with locations of micro-seismicity seen during the tensile phase of the EGS experiment, providing a possible hydrologic connection between EGS well 27-15 and injection/production wells further south-southwest. This FLAC^{3D} hydro-mechanical model will next be coupled to TOUGHREACT to investigate the near-field evolution of reservoir transmissivity associated with thermal, hydraulic, mechanical and chemical processes during all phases of the Desert Peak EGS stimulation.

1. INTRODUCTION

The goal of an Engineered Geothermal System (EGS) is to develop a complex and extensive flow path in hot, but low permeability rocks. The application of EGS at operating hydrothermal reservoirs is intended to convert dry or low-permeability unusable wells into operational injectors or producers, in an attempt to increase field productivity. To develop a complex flow path characterized by large surface area to rock volume ratios, as needed for optimal heat exchange, EGS experiments to date (e.g., Soultz-sous-Forêts, Desert Peak, Newberry, Habanero) have typically used stimulation techniques that enhance the permeability of existing and naturally tortuous fracture networks generally found to be ubiquitous within the crust.

The Desert Peak geothermal field is a successfully operating geothermal field with an approximate 23 MWe output located in the northern portion of the Hot Springs Mountains of northwestern Churchill

County, Nevada, about 100 km northeast of Reno. Well 27-15 was selected to carry out a U.S. Department of Energy supported EGS project with the intent of improving the hydraulic connection with the rest of the reservoir and enhancing overall injectivity. Well 27-15 was originally drilled to a total depth of about 1771m. In 2010 it was back-filled to a total depth of about 1067m, with the completed open-hole section extending from 914m to 1067m to provide a short interval just below the casing shoe, but within the reservoir, to stimulate through hydraulic and chemical methods [2].

Hydraulic stimulation carried out in Desert Peak well 27-15 from September 2010 through April 2011 led to a nearly 60-fold increase in injectivity [2]. This stimulation was carried under two different fluid pressure conditions relative to the least principal stress. An initial period of shear stimulation, which increased injectivity by more than one order of magnitude, from ~0.011 to ~0.15 gpm/psi, was carried out in a series of steps at low fluid pressures up to 4.5 MPa well head pressure (WHP). This maximum WHP was chosen to remain below the magnitude of the least horizontal principal stress (WHP ~5.2 MPa), as measured in this well just below the casing shoe by a mini-hydraulic fracturing test [15]. This low-flow-rate phase was immediately followed by a large-volume controlled hydraulic fracturing operation that lasted more than 23 days, which was carried out at high injection rates and WHP in excess of the least principal stress. This hydraulic fracturing stage resulted in an additional 4-fold increase in injectivity [2]. Temperature-Pressure-Spinner logs show that the injected fluid exited and stimulated well 27-15 at two primary locations: 1) the bottom of the open-hole section during the low-flow-rate injection phase and 2) the hydraulic fracture just below the casing shoe during the high-flow-rate injection phase.

During the EGS experiment, a total of 42 micro-earthquakes (MEQs) with magnitudes ranging from +0.10 to +0.74 were recorded between EGS well 27-15 and injection/production wells to the south-southwest, including in proximity to injection wells 21-2 and 22-22 (see ***Figure 2*** and Figure 3) [2]. All but one of these MEQs occurred during the controlled hydraulic fracturing stimulation, with only one event (discussed below) occurring during shear stimulation. During all stimulation stages, the greatest injectivity gains are associated with the initiation or occurrence of these MEQs under either constant or decreasing wellhead pressure (***Figure 1***). This suggests that shear failure (i.e., faulting) resulting in the generation of MEQs is a key physical process controlling the evolution of transmissivity.

Variations in injection rate occurred in wells 21-2 and 22-22 at various times during the EGS stimulation, especially prior to the controlled hydraulic fracturing stage. In some cases, this makes it difficult to establish a unique correlation between EGS operations and the observed seismicity. However, no significant variations in injection rate were occurring in wells 21-2 and 22-22 when the first MEQ was observed on Sept 17, 2010, during the low-flow-rate shear stimulation (Figure 1). As discussed below, this is one reason this stage of the Desert Peak EGS stimulation was selected for analysis in the present paper.

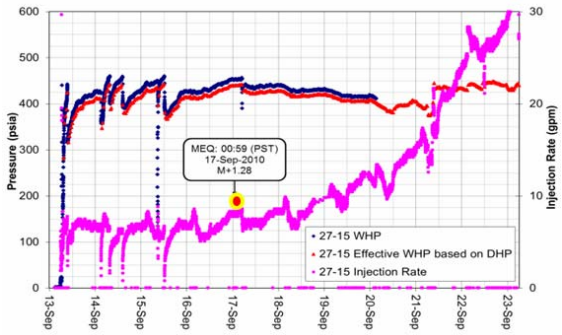

Figure 1: Low-flow rate injection phase, Sept 2010: well 27-15 well-head pressure (WHP) and injection rate. The observed Sept 17 micro-earthquake (MEQ) occurs after about 4 days of injection and it is followed by a remarkable increase in the injection rate under constant wellhead pressure (Figure from [2]).

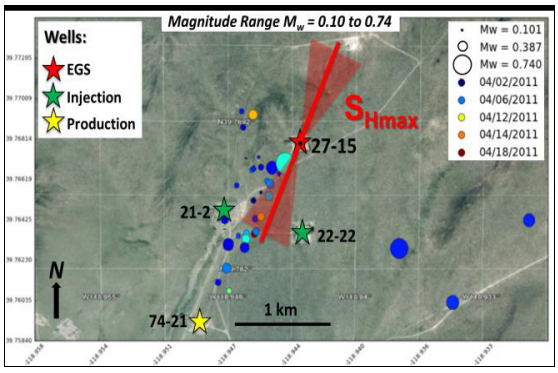

Figure 2 – Map view of the MEQs observed throughout the entire EGS experiment. The events are aligned with the direction of S_{Hmax} (Figure from [2]).

Poor focal sphere coverage and limited constraints on the seismic velocity model make it difficult to: (1) derive the exact source mechanism for these MEQs, (2) detect events smaller than magnitude $M_w < +0.1$ or (3) define the location of individual events with precision. Nevertheless, tensile failure produces relatively high frequency signals at the crack tip – typically of M<<0, which can usually only be

detected with the use of specialized downhole instruments [34]. Thus, it is likely that the primary process generating MEQ events at Desert Peak is hydraulically-induced shear failure (Mode II-III) along pre-existing natural fractures and faults that are well-oriented for shear failure in the regional stress field (see [3] and [15]).

The first goal of this study is to identify any structure that may provide a high permeability conduit enabling connection to the rest of the field, and appearing to be spatially associated with MEQs during the various stimulation phases (all 42 MEQs).

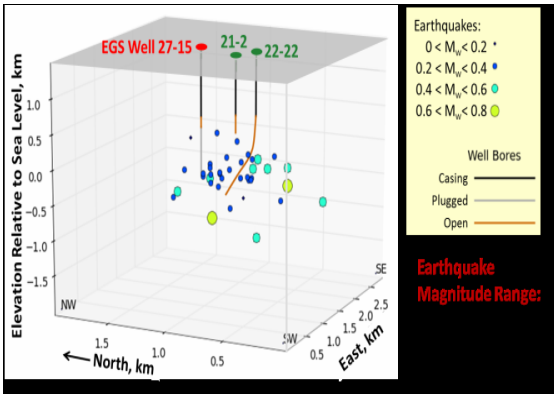

Figure 3 – 3D view of the 42 MEQs observed throughout the entire EGS experiment. The events appear to be clustered at about 1500m depth (Figure from [2]).

The occurrence of MEQs at any stage of the injection phase is critical as: 1) most of the observed MEQs precede strong changes in injectivity during otherwise approximately constant WHP (indicating permeability development/enhancement); 2) The first, and lowest pressure phase of injection is associated with a single MEQ located below the injection interval, but approximately on the same population of MEQs observed during all stimulation phases. This MEQ also immediately precedes large gains in injectivity at near constant WPH in 27-15, which suggests a connection between fluid supplied from 27-15 and the MEQ, and that the MEQ along the flow path from 27-15 to the main field is one of many shear events that caused a reduction in resistance to flow (i.e., a gain in permeability) during the Sept 2010 low-flow-rate injection phase.

The second goal of the study is to numerically simulate whether fluid pressure changes at the location of this MEQ, in response to low-flow-rate injection into 27-15, are sufficient to cause frictional failure. This simulation utilizes: (a) injection rates into 27-15 during the low-flow-rate injection phase (when the single MEQ occurred), (b) a statistical characterization of the fracture population surrounding well 27-15, and (c) the effect on fluid pressure at the MEQ location due to concurrent injection into well 22-22 to the south. Note that the underlying proposition of this consistency test is that the MEQ is causally related to a subsequent change in injectivity. This is accomplished by simulating well-head pressure response during the Sept 2010 low-flow-rate EGS injection phase (Figure 1). The Sept 2010 stimulation phase is a good candidate for our initial model verification and calibration because: a) injection during this phase occurred at pressures below S_{hmin}, thus only shearing processes were involved, b) the injection rate climbs immediately after a single, yet significant, MEQ event and c) injection into nearby wells 22-1 and 22-22 was relatively steady at the time this earthquake occurred, which also coincided with the onset of the pronounced injectivity gain observed in well 27-15 (Figure 1).

Thus, only shear failure is considered and modeled in this paper, as it is the only process occurring during the Sept 2010 injection phase. Tensile failure likely occurs during the subsequent medium to high-flow-rate hydraulic fracturing phases around the open-hole section of well 27-15 at Desert Peak. Such tensile failure is not addressed in this paper and will be part of a future study. Thermal stresses will also be considered in modeling all stages of the Desert Peak EGS stimulation at a later date.

This model presented in this paper is not unique but offers one possible explanation for the deep location of MEQs observed during the Desert Peak EGS stimulation. The observed MEQs seem to be influenced in a complex way by injection operations in both wells 27-15 and 22-22. Although we allow for some injection into well 22-22 in our modeling (see below), this issue is not addressed in detail here but will be addressed in detail in a future study.

2. RESERVOIR CONCEPTUAL MODEL

The Desert Peak geothermal field is located in the northern portion of the Hot Springs Mountains. Extensive drilling in the Desert Peak geothermal area has shown that the Hot Springs Mountains are mainly comprised of Tertiary volcanic and sedimentary rocks that lie directly on Mesozoic metamorphic and granitic basement [10][19]. Intrusive rocks below depths of 2134m have intruded and contact-metamorphosed a Mesozoic sequence of marine metasedimentary and metavolcanic rocks between about 900m and 2200m depth. A Tertiary volcanic section that overlies the pre-Tertiary rocks can be broken into a lower rhyolitic unit composed primarily

of ash-flow tuffs and an upper basaltic unit known as the Chloropagus Formation. The combined thickness of this volcanic package is between 760m and 920m. Overlying these volcanic rocks is a sequence of Pliocene, lacustrine sedimentary rocks known as the Truckee Formation, which is up to 180m thick in the vicinity of the wells. Quaternary alluvium and layers of windblown sand cover most of the surface area in the immediate vicinity of the well-fields [12]. The main Desert Peak reservoir resides in pre-Tertiary rocks [10] (Figure 4).

The Desert Peak geothermal field and the Northern Hot Springs Mountains lie within the NNE-trending Humboldt structural zone, which is orthogonal to the extensional direction of the Walker Lane. On a large scale, the Walker Lane is a system of dextral faults that accommodates ~20% of the relative motion between the Pacific and North American plates [8].

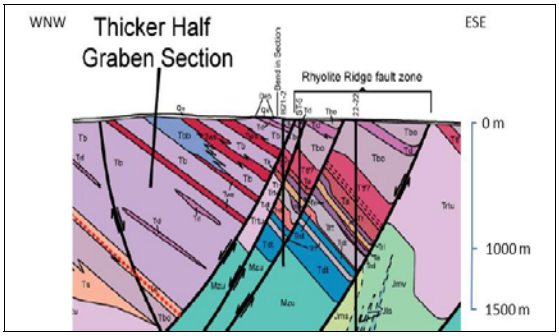

Figure 4: Well 27-15 WNW-trending geologic cross section of the Northern Hot Spring Mountains. Unit abbreviations: Mzu, Mesozoic basement; Jmv, Jls, Jms, Jurassic metamorphic rocks; Trtu, Oligocene tuffs; Tdt, Trt, Oligocene ash-flow tuffs; Trdl, Oligo-Miocene rhyolite-dacite lavas; Trl, Oligo-Miocene rhyolite lavas; Tt, late Oligocene-early Miocene tuff; Ta, early to middle Miocene andesite-dacite lavas; Ttf, middle Miocene ash-flow tuff; Tbo, older basalt lavas; Tbb, basaltic breccia; Td, diatomite; Ts, lacustrine sediments; Tb, basalt lavas; Qe, eolian deposits. (Figure modified from [9]).

The dominant fault pattern trends about N25°E and appears to be related to Basin-and-Range tectonic stresses. The Humboldt structural zone may reflect both strain transfer and extension related to the Walker Lane [10]. The most significant fault in the area is the WNW-dipping Rhyolite Ridge fault zone, which consists of several strands and steps to the left, in the vicinity of the Desert Peak geothermal field [9] (Figure 4 and Figure 5). NW-trending gravity contours across the Desert Peak field may reflect a relay ramp [18] associated with southward-increasing displacement on the Rhyolite Ridge fault zone [9]. Kinematic data gleaned from fault surfaces indicate dip-slip normal displacement on the NNE striking faults and a WNW-trending extension direction, which is compatible with: 1) regional extension directions inferred from geodetic data [13]; 2) borehole tensile failure data and stress magnitudes from a mini hydraulic fracturing experiment; and 3) rock densities consistent with a normal faulting stress regime from wells in the area [3][15] (***Figure 5***).

The most productive area in the system occupies left steps in the NNE-striking, west-dipping normal fault system. Although left stepping oblique- or strike-slip faults are not required for the localization of high permeability (i.e., interactions among normal-faults could also lead to dilatation and locally enhanced fracture permeability in this region) the potential for high fracture density in this step-over region could enhance permeability [9] (*Figure 6*) and is consistent with modeled slip on the Rhyolite Ridge fault [37].

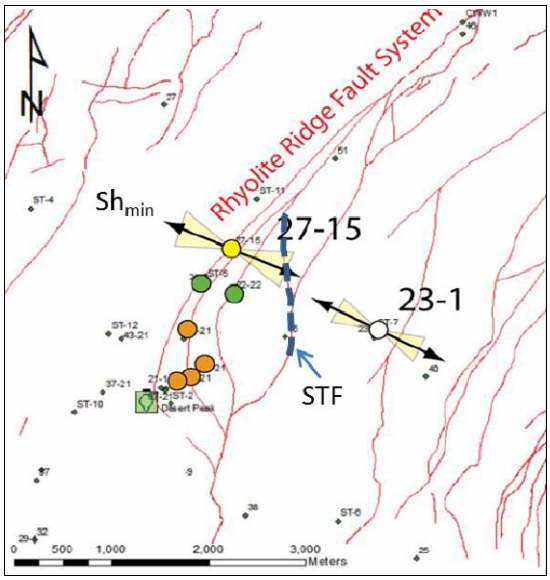

Figure 5: Desert Peak Geothermal Field: a consistent orientation of S_{hmin} is inferred from observations of tensile fractures in wells 27-15 [3] and 23-1 [31]. Production wells are shown in orange, injectors in green, EGS well 27-15 in yellow (Figure modified from [37]). Surface trace of the Shearing Target Fault (STF, discussed below) inferred to intersect wells 22-22 and 27-15 at depth is also shown with a blue dashed line (see explanation below).

Tracer test returns in production well 74-21 from injection in both 21-2 and 22-22 confirm strong hydraulic connectivity in the productive area of the field [32] (Figure 7). In contrast, tracer tests conducted by injecting in well 27-15 and sampling in well 74-21 show only modest connection between 27-15 and the rest of the reservoir [2].

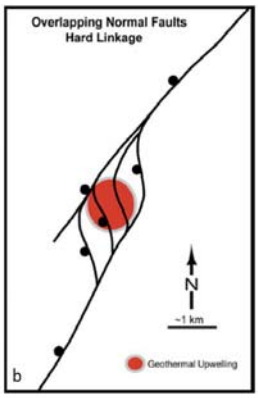

Figure 6: Commercial permeability is encountered in the interpreted left-step of the Rhyolite Ridge Fault Zone [9], where production wells are located. Black dots are shown on downthrown sides of normal faults (Figure from [9]).

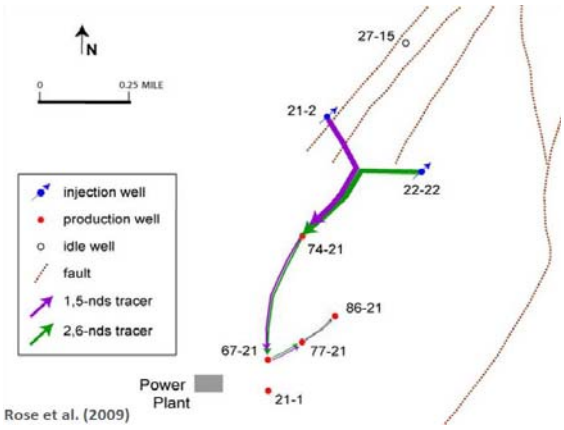

Figure 7: Hydrologic connections (i.e., flow paths) inferred in 2009 by injecting tracers in injection wells 22-22 and 21-2 and sampling in production wells. Results show strong returns to nearest producer 74-21, and slower, weaker returns to other wells. Connection between reservoir and 22-22 occurs through base of Rhyolite Unit and STF (Figure from [32][7]).

Like many other fields, the volume of hot rock surrounding the Desert Peak geothermal field is far more extensive than the volume of hot *and* permeable rock. These circumstances have driven the need for an EGS experiment that can extend the reservoir into untapped hot rock to the north of the field, creating potential new injectors and increasing the residence time of the fluid.

Orientations of the horizontal principal stresses in well 27-15 were determined through analysis of drilling-induced tensile fractures visible in both high-temperature acoustic televiewer (ABI85) and formation micro-scanner (FMS) logs. These drilling-induced structures indicate that the azimuth of the minimum horizontal principal stress, S_{hmin}, is currently oriented 114 ± 17° (corresponding to a maximum horizontal principal stress of 024 ± 17°) [3]. Previous analysis of stress directions from borehole failure observed in well 23-1, located 2km E-SE of well 27-15, is in excellent agreement with stress orientations inferred from well 27-15 [31], suggesting a regionally uniform stress field (***Figure 2*** and Figure 5).

A detailed 3D analysis of the EGS wellsite based on the geologic cross section and map introduced by *Faulds et al., 2010* [9] (***Figure 8*** and ***Figure 10***), suggests that EGS well 27-15 and injector well 22-22 encounter the same permeable horizon at about 1400m depth, which is consistent with a moderate inter-well connection revealed by pressure interference testing (***Figure 9***) [40] and TPS logs [3].

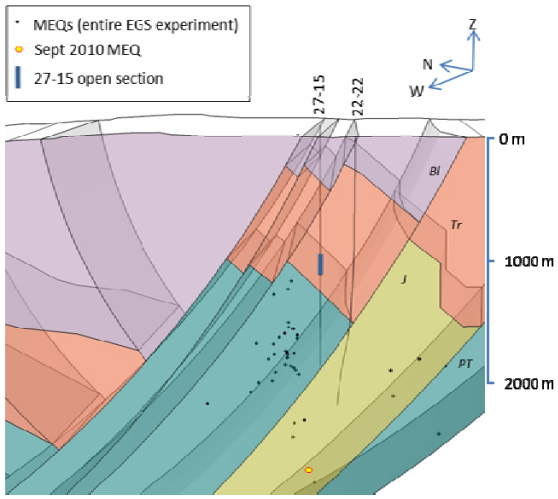

Figure 8: Three dimensional geologic model of EGS wellsite, derived from the geologic cross section and map of Faulds et al., 2010 [9], but with lithology simplified and grouped into fewer units to facilitate conceptual modeling and numerical simulation. Clustering of MEQs (shown from entire EGS experiment) mostly occurs within the Mesozoic and Jurassic metamorphic basement at depth. Unit abbreviations: J, Jurassic metamorphic basement; PT, Pre-Tertiary basement; Tr, Tertiary lavas and ash-flow tuffs; Bl, basalt lavas.

This horizon is the projection at depth of one of the main Rhyolite Ridge Fault Zone structures mapped at the surface, the Shearing Target Fault (discussed below; see Figure 11 and Figure 5), which is also approximately parallel to S_{Hmax}. This fault is near a dense cluster of MEQs associated with injection into well 27-15 and increases in injection rate that were occurring at about the same time into well 22-22.

The temporal association of high-pressure injection into 27-15 during the controlled hydrofrac phase and this cluster of seismicity suggest that the EGS stimulation caused some of this seismicity. However, concurrent increases in the injection rate into well 22-22 immediately before high-pressure injection makes it difficult to establish a unique causal link between most of this seismicity and the EGS stimulation. Also, this seismicity occurs at a depth of 1400 to 1600m, which is significantly below the interval of fluid egress from well 27-15 at a depth of ~914m [2] (***Figure 8***). At 1400m depth, significant fluid loss associated with large-aperture fractures is observed in the deeper section of well 27-15 [3]. Also, in well 22-22, an active injection well located ~400m south of 27-15, major feed zones are found at depths of 790m and 1340m.

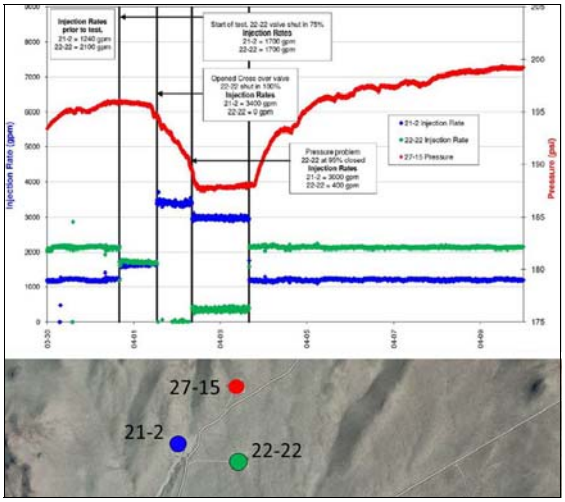

Figure 9 – Transient testing conducted by altering injection rates in wells 22-22 and 21-2 while observing pressure response in well 27-15. The test shows that well 27-15 is weakly but mainly connected with well 22-22 (Figure modified from [7]).

Weak connectivity between wells 27-15 and 22-22 is confirmed by transient hydraulic testing (***Figure 9***) [7], and may be occurring through these deeper fluid loss/feed zones.

Thus, a major NNE-SSW striking and WNW dipping segment of the Rhyolite Ridge Fault Zone might extend between wells 22-22 and 27-15 and establish a cross-formational hydraulic connection between these two wells (Figure 11). This structure appears to represent a preferential flow path for fluids circulating in its vicinity, in addition to being well oriented for shear failure in the current stress field [15] [37]. However, if this structure played a role during the EGS stimulation – as suggested by the deep seismicity observed during both the low- and high-pressure stimulations - a hydrologic connection must have been established between the shallow stimulation interval in well 27-15 and this deeper fault zone. Pressure transient tests (discussed above) indicate that pumping in 22-22 could also contribute to pressurization of this structure (Figure 9), supporting the idea that injection rate changes into well 22-22 just prior to high-pressure (controlled hydraulic fracturing) stimulation might also have contributed to this deep seismicity. The tracer tests suggest that permeability along this structure decreases northward of the injectors (Figure 7), or with increasing distance from the most productive area in the field [32].

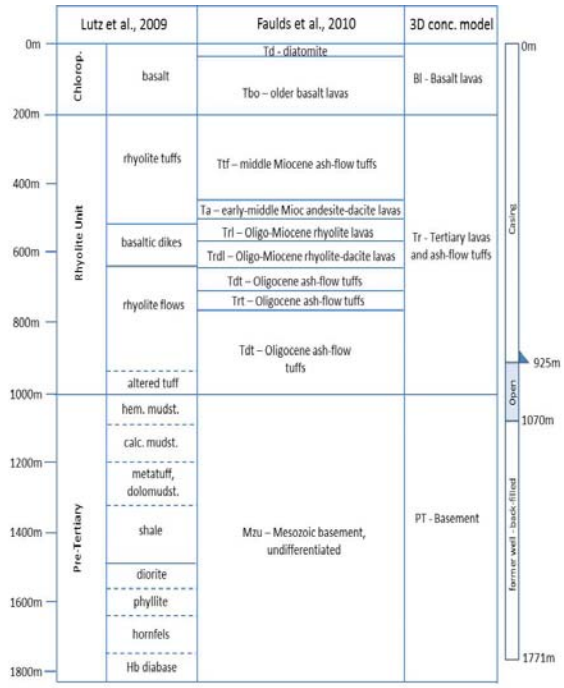

Figure 10: Lithology correlations between available Desert Peak geological models and simplified lithological grouping used for the 3D conceptual model of the wellsite (Figure 8). Well 27-15 schematic diagram is also shown.

Based upon the deep seismicity observed, we propose that this fault segment might have played a significant role in all stages of the EGS stimulation. One purpose of the modeling presented here is to test this hypothesis to see if it is consistent with known structural and stress characteristics of the EGS site and with the pressure response observed during low-flow-rate (shear) stimulation. For simplicity, this fault-segment will be referred to as "STF" *(Shearing Target Fault)* throughout the paper (***Figure 11***).

This conceptual model for a deep hydrologic connection between well 27-15 and wells to the SSW provides the basis to test potential mechanisms

controlling permeability development during the Desert Peak EGS experiment. In particular, both the clustering of microseismicity (including the single event associated with shear stimulation) and the inferred location of the STF are ~500m deeper than the open-hole section stimulated in well 27-15. Yet, migration of injected fluid from the formation surrounding this open-hole section toward the deeper STF might have been facilitated by existing well-oriented fractures. In this scenario, the resulting transmission of hydraulic pressure increase within the STF is presumed to have triggered shear failure of sufficient magnitude to result in observable MEQs, enhancing permeability and fluid pressure transmission along the STF.

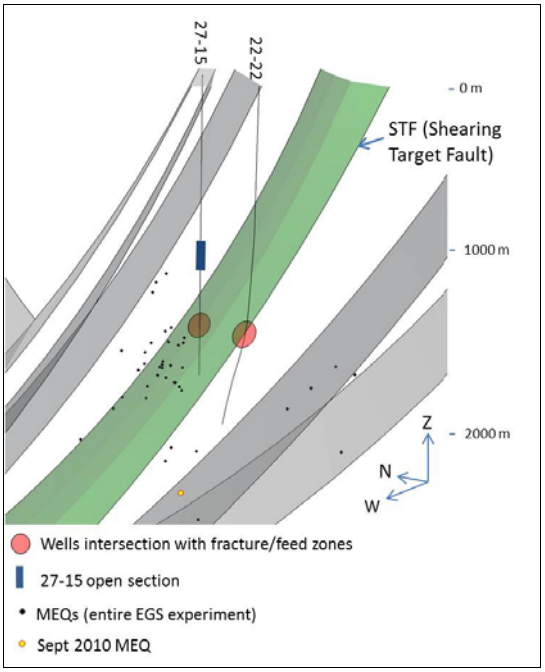

Figure 11: Conceptual model of the major fault strands of the EGS wellsite (inferred from the geologic cross section and map introduced by Faulds et al., 2010 [9]). The three-dimensional geometry allows for a visualization at depth of MEQs (which occurred over the course of the entire EGS experiment) with respect to the structural setting. Both wells 27-15 and 22-22 encounter a highly-fractured and permeable horizon (Shearing Target Fault "STF") at about 1400m depth. Most of the MEQs recorded throughout the course of the EGS experiment are clustered at about 1400m-1600m depth, which coincides with the approximate projection at depth of the STF.

The single MEQ observed during the Sept 2010 phase is located deeper than the main cluster of MEQs observed throughout the entire EGS experiment (Figure 11). However, taking into account significant vertical errors on the order of hundreds of meters for this specific event, the most likely structure which generated the Sept 2010 MEQ remains the STF, which: is independently identified from geological evidence; is known to contain some permeability from previous hydraulic tests; and is also associated with other deep MEQ events during latter stimulation phases.

3. TECHNICAL APPROACH

We investigate whether or not the above conceptual model is consistent with observations made before and during the Desert Peak EGS stimulation by applying statistical and numerical methods to ascertain: 1) the connectivity, attitudes, and hydraulic apertures of pre-existing natural fractures controlling fluid circulation around the EGS stimulation interval, and 2) the potential for initiating shear failure due to fluid over-pressurization that reduces effective normal stress and thus frictional resistance to slip within the STF. This is accomplished through a combination of discrete fracture network (DFN) and hydro-mechanical modeling techniques.

3.1 Discrete Fracture Network Modeling

The study of fracture networks is typically restricted to small, localized sample volumes, and often simplified to 2D. These approaches can provide useful models of the actual fracture network, however, by deriving probabilistic descriptions of fracture location, attitude, spacing, length and aperture from borehole fracture data. The data set measured by *Davatzes and Hickman, 2009* [3] from FMS and ABI85 image logs in well 27-15 is used to generate a representative statistical fracture network to simulate the corresponding fluid flow in the rock volume containing the well. This fracture population spans the interval from 926m to 1705m, and thus extends beyond the limited stimulated open-hole interval (916m to 1067m). This allows us to probabilistically assess the fracture population that extends from the stimulation interval to the STF, which is presumed to host the hydrologic connection. The data set consists of a total number of 567 fractures with associated measured and true vertical depth, attitude (dip and dip direction), apparent aperture (i.e., thickness at the borehole wall in the image logs), and a ranking of the reliability of the fracture identification as well as an assessment of the quality of the image log. The latter provides insight into whether variations in fracture density are related to changes in the fracture population or simply to the quality of the image log [3]. Fractures with immeasurably thin apparent apertures (typically the lowest quality picks), or with a <45° dip angle (probable bedding planes [9] with no preferred

orientation) are not considered in this statistical fracture analysis, as they are less likely to contribute to fluid flow. This results in a total of 261 discrete fractures sampled over a length of 778m to yield a fracture frequency of 0.3 fractures/m and an average fracture spacing of 3m. Table 1 shows the statistical analysis results for the two identified main fracture clusters, with the remaining 29.1% of fractures randomly distributed.

Table 1: statistical parameters used for the generation of the fracture network.

	CLUSTER 1	CLUSTER 2
Quantity	71	114
Cluster Probability	27.2 %	43.7 %
Mean Strike	28.6°	205.9°
Mean dip	58.0°	58.4°
kappa	16.9	12.0

These two antithetic fracture sets are in agreement with structures observed at the field scale. In particular, the principal Cluster 2 is consistent with the main NNE-striking, WNW-dipping Rhyolite Ridge Fault Zone (Figure 12).

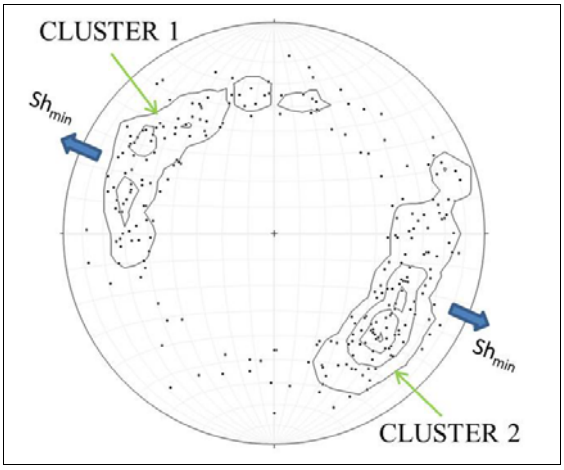

Figure 12: Lower hemisphere, equal area stereographic projection of poles to natural fractures used as input for the DFN simulation (from analysis of image logs along the entire sampled well [3]). Fractures with negligible apparent aperture or with a < 45° dip angle are not shown since not considered in the analysis. The identified clusters show agreement with the observed stress field [15].

The apparent apertures of fractures imaged in well 27-15 represent intervals of reduced resistivity at the borehole wall in the case of FMS images, and in the case of ABI85 images correspond to intervals in which the reflected acoustic pulse is scattered by irregularities in the borehole surface. Apparent aperture values range from millimeters to centimeters and are more representative of fault core thickness [35] than mechanical or hydraulic aperture, which are typically expected to be on the order of microns [22] [4]. Given the limitation of image logs to directly measure hydraulic aperture, we adopt a scaling approach that combines the total number of flowing fractures identified by temperature/spinner anomalies [3] with the permeability-thickness value measured during hydrologic tests to estimate the hydraulic fracture aperture [28].

Temperature/spinner anomalies show evidence of 28 flowing fractures along the entire sampled length (778m), 8 of which are along the stimulated open-hole section of the well (152m) [3]. Along the same open-hole section, a permeability-thickness of 60 mD-ft was determined [36], yielding an average permeability of 1.2e-16 m^2, a hydraulic conductivity of 4.7e-09 m/s (using reservoir fluid properties for a measured temperature of 120°C: fluid density ρ=948.7 kg/m3, fluid viscosity μ=2.35e-04 Pa-s) and a corresponding average transmissivity of 7.1e-07 m^2/s. Considering 8 flowing fractures along the current open-hole section of the well, the equivalent average transmissivity T per flowing fracture becomes 8.9e-08 m^2/s. By applying the cubic law, $b = (12\mu T/\rho g)^{1/3}$, the mean hydraulic aperture b is therefore 30µm.

Borehole data is also limited by the inability to directly measure fracture length, which is critical to assessing the connectivity of fracture networks. In the absence of reliable data relating fracture length to either mechanical aperture for tensile (Mode I) fractures or slip for shear (Modes II, III) fractures [33], fracture length is assumed to be distributed according to a power-law: $P(L \geq l) = Cl^{-a}$, where the power-law exponent a typically ranges from 1 to 3 in naturally-fractured rock masses (e.g., [1] [30]) and C is related to the minimum fracture length. A power-law exponent of a=2, corresponding to the approximate average of power-law exponents measured in the field [30] was selected to represent fracture length in the DFN model. Fracture networks with a=2 consist of an approximately even mixture of short and long fractures [6][14][26][27]. The resulting fracture lengths are then scaled to the fracture heights using a relationship defined for normal faults in layered sequences [23]: $H = \frac{L}{2.2}$, where H and L are the fault height and length, respectively.

From the fracture analysis described above, a three-dimensional DFN is reproduced [29] where fractures are seeded as: 1) fracture location via a random point process, 2) orientation via a Fisher distribution consistent with prior probabilities for each set, 3)

fracture lengths by input of the a=2 value through a Pareto distribution truncated to censor extreme values greater than 200 m; and 4) a lognormal distribution of fracture transmissivity. The 3D DFNs are then projected onto 3 planes (orthogonal to each other) aligned with the Cartesian coordinate system for computation of the conductivity tensor. The lognormal distribution of fracture transmissivity is derived from fracture aperture as follows. Only 8 of 261 fractures (~3%) were found to be significantly conductive, which we define as having a hydraulic aperture greater than 100µm from the well-test analysis presented above. Using a mean fracture aperture of 30µm derived from the well hydraulic test, fracture variance is changed so that approximately 3% of the fractures have an aperture greater than 100µm. The upper and lower bounds of the distribution are then censored to avoid computational problems with apertures being too small (< 2µm) and to retain realness by not allowing apertures to be unreasonably large (>500µm). This censoring affects less than 1% of all generated aperture values.

In order to compute a permeability tensor representative of the background natural fracture population, a 3D DFN was first generated until the fracture frequency of 0.3 fractures per meter derived from image log analysis was achieved within the DFN 200m × 200m × 200m domain (computed along multiple scan lines), followed by projection of these fractures onto three 200m × 200m orthogonal planes aligned with the Cartesian coordinate system: *x*-*y*, *y*-*z*, *x*-*z*. Discrete fracture networks are analyzed for intersection with three fracture types: all fractures, hydraulic backbone fractures, and dominant fractures. "All fractures" refer to all fractures present in a rock mass, whereas "hydraulic backbone" fractures refer only to the interconnected fractures of the hydraulic backbone. The fracture backbone is thus computed for each Cartesian plane by eliminating dead-end segments and isolated clusters, as these cannot contribute to transmissivity. Two configurations of linearly decreasing head conditions are applied to compute each permeability tensor component, and flow is then solved iteratively via a biconjugate gradient method under specific boundary conditions at all internal nodes according to Darcy's law [5][17][25][28][24].

3.2 FLAC^{3D} Fluid-Mechanical Response Model

The conceptual model is tested against the September 13 to 23, 2010, low-flow-rate injection phase (Figure 1) by numerical simulation with the mechanical-flow code FLAC^{3D}.

FLAC^{3D} is a three-dimensional explicit finite-difference program for continuum mechanics computation which also models fluid flow and its corresponding poromechanical effects. [11]

This simulation consists of two successive stages: (1) hydraulic-only computation of pressure gradients generated between the STF and the stimulation interval during fluid injection, and (2) a hydro-mechanically coupled calculation to estimate the mechanical deformation in response to increased hydraulic pressure within the STF, where changes in pore pressure generate deformation, and volumetric strain causes pore pressures to evolve.

As mentioned above, the simpler characteristics of the September 2010 phase make it a perfect candidate for model verification and calibration for subsequent simulation of more complex injection phases, given that: a) injection during the Sept 2010 phase occurs at pressures below S_{hmin}; and b) the injection rate climbs immediately after detection of a single, yet potentially significant, MEQ event. This suggests the process triggering the MEQ event plays a primary role in transmissivity development during this phase. The timing at which this single MEQ occurred represents a perfect reference for model calibration as it defines the diffusion time required by the hydraulic pressure to build-up to a value critical for triggering mechanical deformation (i.e. shear failure) in the rockmass. Therefore, we tune the model of pressure diffusion through the fracture network between the open-hole interval in 27-15 and the location of the MEQ, presumed to be on the STF, to determine the model parameters/conditions necessary to cause an MEQ 4 days after the initiation of injection into 27-15 at WHP fluid pressures of ~3.2MPa. In this case, pressure sufficient to reduce effective normal stress must be communicated to the STF in order to satisfy the conditions for Mohr-Coulomb failure. The 27-15 Sept 2010 low-flow-rate injection is used to verify these conditions.

As introduced above, injection into 27-15 is not the only source of pressure perturbation in the studied area. Injection into 22-22 has also a potential connection to this volume, and flow was varied into this well during the EGS experiment. However, during the Sept 2010 low-flow-rate phase, fluid from 22-22 was transferred to 27-15, and thus injection in 22-22 consisted of about half the rate injected in 27-15, at approximately four times less than the 27-15 injection pressure.

In addition, this MEQ occurring approximately 4 days after the initiation of injection is a good reference when calibrating the model, as it represents the time over which the hydraulic pressure diffusion

process builds up and triggers the shear mechanism. The 27-15 low-flow-rate phase allows for a sensitive and accurate calibration of the pressure gradient throughout the STF zone. Finally, influence from injection operations in well 22-22 is limited during this phase, consisting of about half the rate injected in 27-15, at approximately four times less than the injection pressure.

For both simulations, and as a general rule, the simplest possible geometry option is used to define the FLAC^{3D} model, consistent with the reproduction of key physical processes. In the simplified representation of the wellsite, the model comprises a low permeability background formation, two injection points (wells 27-15 and 22-22) and a NNE-striking fault zone (STF) about 100m thick, dipping 70° WNW and located about 500m below the actual 27-15 injection point. The model domain extends for 3000m in the x-direction, 700m in the y-direction and 2600m in the z-direction. The grid is discretized into regular cubic zones 100m on a side. The STF - like the rest of the model - is currently assumed to be a fluid-saturated single-porosity media. Later modeling exercises involving coupling with TOUGHREACT may adopt a dual-porosity conceptualization.

A phreatic surface is initialized at 118m depth, below which pore pressures have a constant gradient once the initial force-equilibrium state is reached. (in FLAC^{3D}, force-equilibrium is assumed when the maximum unbalanced force and velocity vectors at each gridpoint are small compared to the representative zone forces in the problem). Realistic hydraulic conditions typical of a fractured reservoir are represented in the model by anisotropic permeability. For numerical purposes, the lithological units described in Section 2 are grouped into rock types (a) through (c) as: a) corresponding to both the basement and the rhyolite units and representing the background rock mass; b) simulating the rock behavior in the vicinity of the open-hole section of the well, and c) representing the STF.

The permeability assigned to the formation surrounding well 27-15 in the FLAC^{3D} model is guided by the DFN equivalent permeability tensors computed from site-specific fracture attributes. A higher vertical permeability (k_z) is used to simulate an assumed vertical connection between the open-hole interval of 27-15 and the underlying STF (rock type b). The highest permeability values are assigned to the STF, within which both the vertical and horizontal tensors vary according to a prescribed gradient between well 27-15 (STF north end) and well 22-22 (STF south end) (Table 3). The STF permeability gradient is being assigned and adjusted by calibration against: 1) instantaneous downhole pressure in well 27-15 and 2) pressure transient testing carried out between wells 27-15 and 22-22.

The low background permeability of the formation guarantees that fluid flows preferentially through the STF and eventually exits the model to the south, toward the productive area of the field. The model is set by using permeable boundary conditions (i.e., the pressure is set to remain constant at the boundaries of the model after the initial equilibrated pressure is reached). Velocity and displacements are fixed at the bottom and sides of the model (i.e., no velocity or displacement is allowed at the selected gridpoints).

Consistent with the normal faulting regime observed in the field and using the measured magnitude of S_{hmin} [15], xx, zz and yy stress components vary with depth following the relations between S_{hmin}, S_{Hmax} and S_v (vertical overburden): $S_{Hmax} = (S_{hmin} + S_v)/2$ [15]. A Mohr-Coulomb plasticity constitutive model is used in FLAC^{3D} to properly represent the onset of shear (frictional) failure. The failure envelope for this constitutive model corresponds to a Mohr-Coulomb criterion (shear yield function with tension cutoff) which is expressed in terms of principal stresses σ_1, σ_2 and σ_3. For the Mohr-Coulomb plasticity model, the required properties defined for each material are: 1) bulk and shear moduli; 2) friction and dilation angles; 3) cohesion; and 4) tensile strength. The constitutive behavior and associated material properties dictate the type of response the model will display upon disturbance by the injected fluid [11].

The mechanical parameters used in the model are derived from rock mechanical tests conducted on selected core samples representative of the stimulation interval in well 27-15 [20]. Mechanical properties for the Rhyolitic and Metamorphic Basement Units are averaged and assigned to rock types a, b and c. A lower friction angle of 22° is used for rock type c (Table 2). The latter is also set with zero cohesion, as in-situ stress measurements in a variety of tectonically-active geologic settings suggest that fracture planes well oriented with respect to the stress field are generally cohesionless [14][39].

Table 2: Mechanical properties used in the FLAC^{3D} hydro-mechanical model.

	Rock type a, b	Rock type c
Density [g/cm^3]	2.5	2.5
Shear Modulus [MPa]	1.0E+04	1.0E+04
Bulk Modulus [MPa]	1.7E+04	1.7E+04
Friction angle [°]	39.1	21.0
Cohesion [MPa]	20.6	0
Tensile strength [MPa]	1.0E+04	1.0E+04

Boundary and initial conditions define the *in-situ* state (i.e., the condition before a change or disturbance is introduced by injection). After these conditions are defined in FLAC^{3D} and the initial equilibrium state is calculated for the model, an alteration is made (e.g., a change in pore pressure at selected points), and the resulting model response is computed. For both hydraulic-only and hydro-mechanical simulations, a prescribed volumetric inflow of fluid varying with time is assigned to define the principal fluid sources in the model (wells 27-15 and 22-22).

Table 3: Anisotropic permeabilities used in FLAC^{3D}.

	kx [m^2]	ky [m^2]	kz [m^2]	Porosity φ
Rock type a	1.4e-16	1.4e-16	7.2e-18	0.01
Rock type b	1.9e-17	1.9e-17	7.0e-17	0.01
Rock type c (27-15 end)	7.0e-18	1.0e-17	1.9e-14	0.01
Rock type c (22-22 end)	7.0e-16	2.3e-14	9.4e-17	0.01

An average volumetric flow rate of 5e-5m^3/s is applied to the gridpoints corresponding to the open-hole section in well 27-15. At the same time, an average volumetric flow rate of 2.5e-5m^3/s is applied to the gridpoints corresponding to the two feed zones in well 22-22: 60% of the injected fluid is prescribed to the deep feed zone (basement), while the remaining 40% is applied to the shallower feed zone (rhyolite), which is consistent with temperature-pressure-flowmeter logs run in this well.

4. RESULTS

4.1 Discrete Fracture Network Modeling

Figure 13***a*** provides a 3D representation of the discrete fracture network generated using the procedure described above from the site-specific statistics in well 27-15. The 3D DFNs are projected onto planes aligned with the Cartesian coordinate system for computation of the conductivity tensor. 2D illustration of the relative contribution to flow among fractures on the x-z plane is shown in Figure 13***b***. The DFN correctly reproduces the regional structural trends observed at the field scale from surface mapping, the fracture attitudes from borehole observations, as well as the density of hydraulically-conductive fractures (i.e. 4/100m) identified from TS anomalies in the borehole log data [9]. Geometric and flow techniques eliminate dead-end segments or isolated clusters, and identify the hydraulic backbone representing the interconnected subset of fractures responsible for conducting flow across the model [26][27]. By computing hydraulic conductivity from fracture apertures according to the cubic law for each principal direction (x, y and z), a total of 40 simulations of fluid flow through the generated DFN provide the following horizontal (k_x=east-west, k_y=north-south) and vertical (k_z) average equivalent permeabilities comprising, for the volume containing well 27-15, the permeability tensor k_x=2.50-17m^2, k_y=1.83e-16m^2, k_z=6.16e-17m^2 respectively. The resulting permeability magnitude k is equal to 1.94e-16 m^2. Despite the lack of calibration of the DFN simulations to the measured permeability to date (i.e., only the permeability distribution is conditioned to general observations from hydraulic testing), the results are in very good agreement with the on-site measured permeability of 1.2e-16 m^2 for the formation surrounding the open-hole section of the well [36].

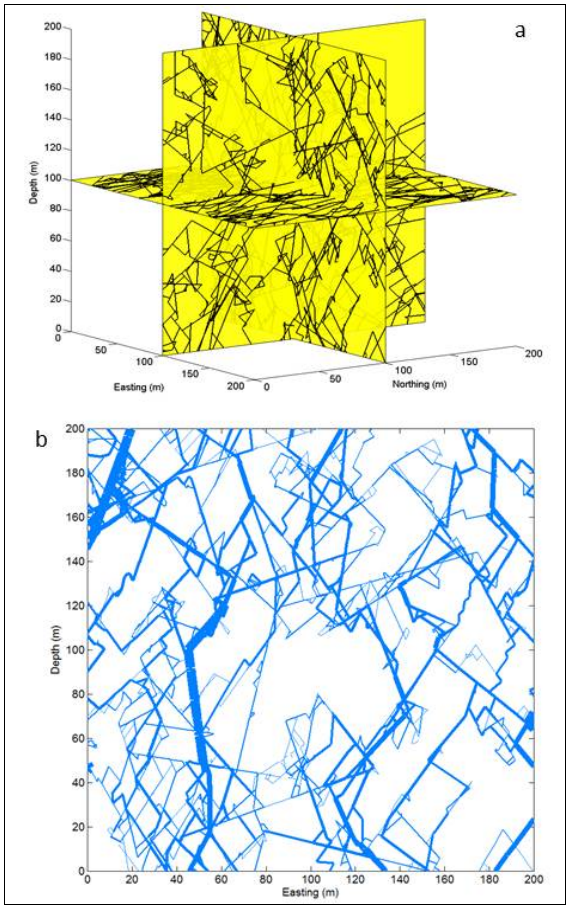

Figure 13: a) Site representative 3D fault network mapped onto three orthogonal planes of a Cartesian coordinate system along with b) fault network projected onto x-z plane with line thickness proportional to flow. Only interconnected fault segments of the hydraulic backbone are shown. Note that the frequency of higher permeability fractures is consistent with that encountered in well 27-15 (i.e., approximately 7 fractures over a 200 m vertical length).

The results emphasize preferential flow through k_y and k_z relative to k_x, in accordance with the trends of the major structural features. The existing natural fracture network supports vertical fluid flow and represents a preferential pathway through which injected fluids can reach greater depths.

4.2 FLAC^{3D} Modeling

In the first set of simple models, only fluid diffusion along fractures in a rigid rock mass was considered. The computationally-simpler hydraulic-only model was necessary in the first stage to estimate if a pressure gradient/incremental could be generated between the STF and the stimulation interval under the Sept 2010 injection phase conditions. The resulting computed pressure incremental was then analytically tested against a Mohr-Coulomb analysis to verify if the resulting pressure incremental could satisfy conditions for shear failure on well-oriented sets of fractures.

Under the prescribed conditions, the FLAC^{3D} hydraulic-only (no deformation in a rigid rock mass) simulation shows that fluid diffusion throughout the STF generates a maximum pressure increase of ~1.8 MPa within the STF after about 4 days of injection (Figure 14).

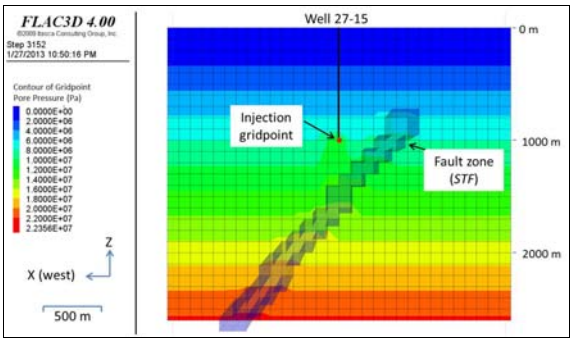

Figure 14: The Sept 2010 low-flow-rate EGS injection phase is simulated in a FLAC^{3D} hydraulic-only analysis by applying constant injection of fluid (5e-5m^3/s) at the injection gridpoint (closest point to the casing shoe of the well) during the EGS stimulation. Fluid diffusion through natural fracture networks from the injection point toward greater depths increases the pore pressure within the more permeable STF. Maximum pressure increase (i.e delta P) simulated within the STF is 1.80 MPa.

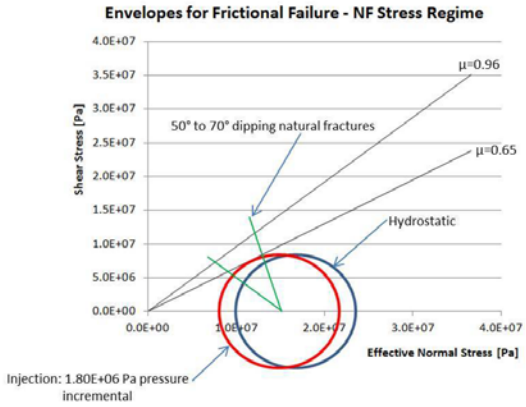

Figure 15 - Normal-stress regime Mohr circles showing shear and effective normal stress at 1600m depth (location of MEQs and STF) under: 1) hydrostatic conditions defined by groundwater level at 118m depth (blue circle) and 2) hydraulic pressure generated along the STF after 4 days of fluid injection in 27-15 (red circle), using pressure increase derived from the FLAC^{3D} hydraulic model (Figure 14). Frictional failure lines are based on the coefficient of sliding friction derived from laboratory testing of rock samples from surrounding geologic units [20]. In-situ natural and cohesionless fractures are well-oriented and critically stressed for shear failure under the Sept 2010 low-flow-rate phase hydraulically-induced conditions.

A Mohr-Coulomb analysis suggests that this maximum pressure increase within the STF is sufficient to generate shear failure in well-oriented, cohesionless fractures (Figure 15).

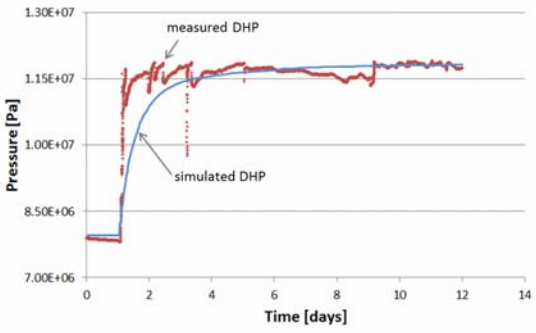

Figure 16: FLAC^{3D} simulated downhole pressure against downhole pressure response observed in well 27-15 during the Sept 2010 low-flow-rate EGS injection phase.

The timing required by the DHP to reach a steady value (instantaneous timing pressure response) as well as the maximum pressure, provide key information on the transmissivity of the formation surrounding the open section of the well. The instantaneous downhole pressure response measured in 27-15 during the injection test is simulated through

inverse modeling exercises and variation of the formation permeability, until a good approximation is reached. This is a promising sign that the correct calibration of the FLAC^{3D} model has been achieved (Figure 16). The FLAC^{3D} hydro-mechanical coupled analysis predicts shear failure within the STF after about 4 days of injection into the stimulation zone of well 27-15. This failure is manifest as a contiguous line of active shearing zones in which the stresses satisfy the yield criterion, denoting that frictional failure is occurring over a zone that is elongated in the down-dip direction (***Figure 17***).

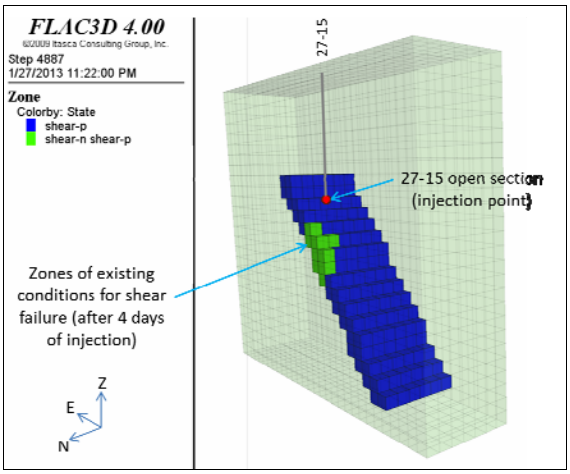

Figure 17: FLAC^{3D} coupled hydro-mechanical simulation of mechanical response as a result of pressure increase generated along the STF during the Sept 2010 low-flow-rate EGS injection phase. FLAC^{3D} displays zones of the model (i.e. STF) where the pore pressure incremental establishes conditions for the initiation of plastic flow (i.e. shear-n > the zone is at active failure now, -n).

5. DISCUSSION AND CONCLUSION

In an attempt to offer a plausible explanation for the location of deep MEQs and to define plausible mechanisms governing the evolution of transmissivity during the EGS experiment, the present study analyzes: 1) 3D site-specific geometry of the key structures involved in the experiment, 2) 3D equivalent permeability tensors in a representative DFN consistent with observations of the fracture network and, specifically, hydraulically conductive fractures within well 27-15, 3) a hydraulic model of fluid pressure distributions within the STF, and 4) a hydro-mechanical simulation consistent with the activation of hydraulically-induced shear failure along the STF.

As introduced above, the MEQ cluster observed throughout the entire EGS experiment is mainly used for structural identification purposes here. The numerical simulation refers to the Sept 2010 injection phase only, when injection operations in 22-22 were reduced and only 1 MEQ was observed. The complexity resulting from combined injection operations at higher-flow-rates is not addressed here and may be discussed in a future study.

The conceptual and numerical modeling results reveal that conditions necessary for fluid "channeling" to depths below the stimulation interval during the Sept 2010 EGS injection phase in well 27-15 can lead to pressurization and poromechanical stressing of the STF. The computed DFN permeability tensors indicate that, within the background natural fracture network, fluid injected at the open section in well 27-15 flows preferentially toward the NNE and the vertical directions (in accordance with the regional structures observed on site).

Two FLAC^{3D} simulations are carried out separately: 1) the hydraulic-only model is run to simulate fluid diffusion and STF pressurization under the Sept 2010 injection phase hydraulically-induced conditions, and the resulting pressure incremental is used as input to the Mohr-Coulomb analytical analysis; 2) the subsequent coupled hydro-mechanical model is run to test the mechanical response of the model and verify conditions for deformation and initiation of shear failure along the STF. The FLAC^{3D} hydraulic-only model is initialized on the basis of the computed DFN permeability tensors and by assigning a higher permeability to the STF. With these conditions, the simulated injected fluid (Sept 2010 phase) migrates from the open section in well 27-15 toward greater depths and it diffuses within the STF. The FLAC^{3D} hydraulic-only model shows localized pressurization of the STF and pore pressure incremental up to 1.8 MPa. Analysis of the resulting effective pressure through analytical Mohr-coulomb circles and FLAC^{3D} hydro-mechanical modeling suggest that these pressures can establish conditions for shear failure within the STF. The injected fluid being colder and denser tends to flows toward the bottom of the STF, generating higher pressure at greater rather than shallower depth within the STF. The subsequent FLAC^{3D} coupled hydro-mechanical numerical model demonstrates that effective stress changes induced by these fluid pressure increases and spatially variable permeability along the STF are sufficient to produce slip and microseismicity within the STF itself. The activation of shearing after about 4 days of injection is also in good agreement with the time at which the single MEQ event is observed during the low-flow-rate injection phase, suggesting a correlation between slip on the deep STF and the Sept 2010 change in injectivity.

The modeling results (i.e. migration of injected fluid at depth, pressurization and shearing of the STF) appear to validate the hypothesis that the proposed framework (based on the identification of the STF) is a plausible explanation for the presumed correlation between the observed injection rate increase and the occurrence of microseismicity at depths greater than the open section. The parameters under which the models simulate this process for the Sept 2010 phase are listed in Table 2 and 3. Shear failure appears to be more sensitive to variations in the STF friction angle.

The identified STF satisfies some of the conditions that are necessary for shear failure initiation: 1) adequate initial transmissivity, (2) optimum orientation with respect to the local stress state, and (3) enhanced transmissivity with slip [21]. Related physical processes have been inferred in several injection-disposal operations, especially along faults that transit between basement rocks and overlying aquifers. Such a process may have been responsible for recent observations of injection-induced seismicity at Guy, Arkansas [16].

Both numerical (coupled hydro-mechanical) and analytical (mechanical Mohr-Coulomb analysis) results support the existence of regions in the STF which can undergo shear failure under the simulated injection-induced hydraulic pressure conditions. Given the non-uniqueness of the problem, the presented conceptual framework is one possible model for the Desert Peak EGS experiment. Future coupling of thermo-hydro-mechanical-chemical processes will be carried out to better understand the evolution of permeability throughout the Desert Peak EGS stimulation.

6. ACKNOWLEDGEMENTS

This work is supported by the Great Basin Center for Geothermal Energy under a Geothermal Technology Program (GTP) Faculty Seed Grant, Ormat Technologies, Inc., and Itasca through the Itasca Education Partnership program. The first two authors wish to acknowledge Belinda Poli for providing comments/feedback while reviewing the document. The same study was presented at the 38th Workshop on Geothermal Reservoir Engineering held at Stanford University, Feb 11-13, 2013.

REFERENCES

[1]. Bonnet, E., O. Bour, N.E. Odling, P. Davy, I. Main, P. Cowie, and B. Berkowitz (2001), Scaling of fracture systems in geologic media, Rev. Geophys., 39(3), 347-383.

[2]. Chabora, E., Zemach, E., Spielman, P., Drakos, P., Hickman, S., Lutz, S., Boyle, K., Falconer, A., Robertson-Tait, A., Davatzes, N.C., Rose, P., Majer, E., Jarpe, S., (2012), Hydraulic stimulation of well 27-15, Desert Peak Geothermal Field, Nevada, USA, *Proceedings, 37th Workshop on Geothermal Reservoir Engineering*, Stanford University, Stanford, California, January 30 - February 1, 2012, SGP-TR-194.

[3]. Davatzes, N.C. and Hickman, S., (2009), Fractures, stress and fluid flow prior to stimulation of well 27-15, Desert Peak, Nevada, EGS project, *Proceedings, 34th Workshop on Geothermal Reservoir Engineering*, Stanford University, Stanford, California, February 9-11, 2009 SGP-TR-187.

[4]. Davatzes, N.C., and Hickman, S.H. (2010), Stress, fracture, and fluid-flow analysis using acoustic and electrical image logs in hot fractured granites of the Coso geothermal field, California, U.S.A., *in M. Poppelreiter*, C. Garcıa-Carballido, and M. Kraaijveld, eds., Dipmeter and borehole image log technology: AAPG Memoir 92, Ch 24., p. 1 – 35.

[5]. de Dreuzy, J.R. & Erhel, J., (2003), Efficient algorithms for the determination of the connected fracture network and the solution to the steady-state flow equation in fracture networks, *Comput. Geosci.*, Vol. 29, No. 1, 107–111.

[6]. de Dreuzy, J.R.; Davy, P. O.and Bour, (2001), Hydraulic properties of two-dimensional random fracture networks following a power-law length distribution: 1. Effective connectivity, *Water Resour. Res*., Vol. 37, No. 8, 2065-2078.

[7]. Drakos, P., Ormat Nevada Inc., (2010), Desert Peak EGS Project, *Geothermal Technologies Program 2010 Peer Review*, DOE: DE-FC6-02ID14406, May 18, 2010.

[8]. Faulds, J.E., and Henry, C.D., (2008), Tectonic influences on the spatial and temporal evolution of the Walker Lane: an incipient transform fault along the evolving Pacific-North American plate boundary, *in Spencer, J.E., and Titley, S.R., eds., Ores and orogenesis: CircumPacific tectonics, geologic evolution, and ore deposits*, Arizona Geological Society Digest 22, p. 437-470.

[9]. Faulds, J.E., Coolbaugh, M.F., Benoit, D., Opplinger, G., Perkins, M., Moeck, I., Drakos, P., (2010), Structural controls of geothermal activity in the Northern Hot Spring Mountains, Western Nevada: the tale of three geothermal systems (Brady's, Desert Peak, and Desert Queen), *Geothermal Resources Council Transactions,* Vol. 34, 2010.

[10]. Faulds, J.E., Garside, L.J., Johnson, G.L., Muehlberg, J., Oppliger, G.L., (2002), Geologic setting and preliminary analysis of the Desert Peak-Brady Geothermal Field, Western Nevada, *Geothermal Resource Council Transactions*, 2002.

[11]. FLAC^{3D} Fast Lagrangian Analysis of Continua in 3 Dimensions, (2009), *User's Guide,* Itasca Consulting Group Inc.

[12]. Goyal, K.P., Benoit, W.R., Maas, J.P., Rosser, J.R., (1983), Desert Peak: a geothermal field in Churchill County, Nevada, *Proceedings Ninth Workshop Geothermal Reservoir Engineering*, Stanford University, Stanford, California, December 1983 SGP-TR-74.

[13]. Hammond, W.C., and Thatcher, W., (2004), Contemporary tectonic deformation of the Basin and Range province, western United States: 10 years of observation with the Global Positioning System, *Journal of Geophysical Research,* v. 109, B08403, doi: 10.1029/2003JB002746.

[14]. Hickman, S. (1991), Stress in the lithosphere and the strength of active faults, *U.S. National Report to the International Union of Geodesy and Geophysics 1987-1990, Reviews of Geophysics*, v. 29, p. 759-775.

[15]. Hickman, S. and Davatzes, N.C., (2010), In-situ stress and fracture characterization for planning of an EGS stimulation in the Desert Peak Geothermal field, Nevada, *Proceedings, 35th Workshop on Geothermal Reservoir Engineering*, Stanford University, Stanford, California, February 1-3, 2010 SGP-TR-188.

[16]. Horton, S., (2012), Disposal of hydrofracking waste fluid by injection into subsurface aquifers triggers earthquake swarn in central Arkansas with potential for damaging earthquake, *Seismological Research Letters*, Vol. 83, Number 2, March/April 2012.

[17]. Klimczak, C., Schultz R.A., Parashar R., Reeves D.M., (2010), Cubic law with correlated aperture to length and implications for network scale fluid flow, *Hydrogeology Journal*, doi:10.1017/s10040-009-0572-6.

[18]. Larsen, P.H., (1988), Relay structures in a lower Permian basement-involved extensional system, East Greenland, *Journal of Structural Geology*, v.10, p 3-8.

[19]. Lutz, S., Moore, J., Jones, C., Suemnicht, G., and Robertson-Tait, A., (2009), Geological and structural relationships in the Desert Peak Geothermal System, Nevada: Implications for EGS development, *Proceedings 34th Workshop on Geothermal Reservoir Engineering*, Stanford, University, Stanford, CA, SGP-TR-187.

[20]. Lutz, S.J., Hickman, S., Davatzes, N., Zemach, E., Drakos, P., Robertson-Tait, A., (2010), Rock mechanical testing in support of well stimulation activities at the desert Peak geothermal field, Nevada, *Geothermal Resources Council Transactions*, Vol. 34, 2010.

[21]. McClure, M., Horne, R., Is pure shear stimulation always the mechanism of stimulation in EGS?*, Proceedings, Thirty-eight Workshop on Geothermal Reservoir Engineering*, Stanford University, Stanford, California, February 11-13, 2013, SGP-TR-198.

[22]. National Research Council, (1996), Rock Fractures and Fluid Flow: Contemporary Understanding and Applications, *National Academy of Sciences*, New York, 551 p.

[23]. Nicol, A., Watterson, J., Walsh, J., Childs, C., (1996), The shapes, major axis orientations and displacement patterns of fault surfaces, *Journal of Structural Geology*, Vol. 18, No. 2/3, pp. 235 to 248, 1996.

[24]. Parashar, R. and Reeves D.M. (2012), On iterative techniques for solving flow in large two-dimensional discrete fracture networks, *Journal of Computational and Applied Mathematics*, doi:10.1016/j.cam.2012.02.038.

[25]. Priest, S.D., (1993), *Discontinuity Analysis of Rock Engineering*, Chapman and Hall, London.

[26]. Reeves, D.M., Benson, D.A., Meerschaert, M.M., (2008a), Transport of conservative solutes in simulated fracture networks: 1. Synthetic data generation, *Water Resour. Res.*, Vol. 44, No. W05401, doi:10.1029/2007WR006069.

[27]. Reeves, D.M., Benson, D.A., Meerschaert, M.M., Scheffler, H.-P, (2008b), Transport of conservative solutions in simulated fracture networks: 2. Ensemble solute transport and the correspondence to operator-stable limit distributions, *Water Resour. Res.*, Vol. 44, No. W05410, doi:10.1029/2008WR006858.

[28]. Reeves, D.M., Parashar, R., Zhang, Y., (2012), Hydrogeologic characterization of fractured rock masses intended for disposal of radioactive waste, *Radioactive Waste*, Dr. Rehab Abdel Rahman (Ed.), ISBN: 978-953-51-0551-0, InTech.

[29]. Reeves, D.M., Pohll, G., Lyles, B., Faulds, J., Louie, J., Ehni, B., Kratt, C., Cooper, C., Parashar, R., Pullammanappallil, S., Noel D.,

(2012), Geothermal resource characterization and evaluation at Astor Pass, Nevada, *Geothermal Resources Council Transactions*, 36, 1371-1376.

[30]. Renshaw, C.E. (1999). Connectivity of joint networks with power law length distributions, Water Resour. Res., 35(9), 2661-2670.

[31]. Robertson-Tait, A., Lutz, S.J., Sheridan, J., and Morris, C.L. (2004), Selection of an interval for massive hydraulic stimulation in well DP 23-1, Desert Peak East EGS project, Nevada, *Proceedings, 29th Workshop on Geothermal Reservoir Engineering*, Stanford University, Stanford CA, SGP-TR-175.

[32]. Rose, P., Leecaster, K., Drakos, P., Robertson-Tait, A., Tracer testing at the Desert Peak EGS Project, *Geothermal Resource Council Transactions*, Vol. 33, 2009.

[33]. Schultz, R.A., Soliva, R., Fossen, H., Okubo, C.H., Reeves, D.M., (2008), Dependence of displacement-length scaling relations for fractures and deformation bands on the volumetric changes across them, *Journal of Structural Geology* 30 (2008) 1405-1411.

[34]. Sherburn, S. and Quinn, R., (2012), An Assessment of the Effects of Hydraulic Fracturing on Seismicity in the Taranaki Region, *GNS Science Consultancy Report 2012/50*, February 2012.

[35]. Shipton, Z.K., Soden, A.M., Kirkpatrick, J.D., Bright, A.M., Lunn, R.J., (2006), How thick is a fault? Fault-Displacement-Thickness scaling revisited, in Abercrombie, R., (Eds) Earthquakes: Radiated energy and the physics of faulting, pp. 193-198, *AGU bulletin,* 2006.

[36]. Stacey, R.W., Robertson-Tait, A., Drakos, P., Zemach, E., (2010), EGS stimulation of well 27-15, Desert Peak geothermal field, Nevada, *Geothermal Resource Council Transactions*, Vol. 34, 2010.

[37]. Swyer, M.W., Davatzes, N.C., (2012), Using boundary element modeling of fault slip to predict patterns of stress perturbation and related fractures in geothermal reservoirs and explore parameter uncertainty, *Proceedings, Thirty-Seventh Workshop on Geothermal Reservoir Engineering*, Stanford University, Stanford, California, January 30 – February 1, 2012, SGP-TR-194.

[38]. Taron, J., Elsworth, D., Min, K.B., (2009), Numerical simulation of thermal-hydrologic-mechanical-chemical processes in deformable, fractured porous media, *International Journal Rock Mechanics & Mining Sciences 2009*, doi: 10.1016/j.ijrmms.2009.01.008.

[39]. Townend, J., and Zoback, M. D. (2000), How faulting keeps the crust strong, *Geology*, v. 28, p. 399–402.

[40]. Zemach, E., Drakos, P., Robertson-Tait, A., Lutz, S.J., (2010), Feasibility evaluation of an "in-field" EGS project at Desert Peak, Nevada, USA, *Proceedings World Geothermal Congress*, Bali, Indonesia, 25-29 April 2010.